APPLIED SCIENCES AND ENGINEERING

Silicon nanomembrane phototransistor flipped with multifunctional sensors toward smart digital dust

Gongjin Li[1]*, Zhe Ma[2]*, Chunyu You[1]*, Gaoshan Huang[1], Enming Song[1,3], Ruobing Pan[1], Hong Zhu[1], Jiaqi Xin[1], Borui Xu[1], Taeyoon Lee[4], Zhenghua An[5], Zengfeng Di[2], Yongfeng Mei[1,4]†

The sensing module that converts physical or chemical stimuli into electrical signals is the core of future smart electronics in the post-Moore era. Challenges lie in the realization and integration of different detecting functions on a single chip. We propose a new design of on-chip construction for low-power consumption sensor, which is based on the optoelectronic detection mechanism with external stimuli and compatible with CMOS technology. A combination of flipped silicon nanomembrane phototransistors and stimuli-responsive materials presents low-power consumption (CMOS level) and demonstrates great functional expansibility of sensing targets, e.g., hydrogen concentration and relative humidity. With a device-first, wafer-compatible process introduced for large-scale silicon flexible electronics, our work shows great potential in the development of flexible and integrated smart sensing systems for the realization of Internet of Things applications.

INTRODUCTION

CMOS (complementary metal-oxide semiconductor) technology has developed rapidly since its invention following Moore's law, and now the advance is accelerated with the requirement of More Moore and More than Moore. With More Moore, the expanding frontier of semiconductor technology mainly focuses on the miniaturization of integrated circuit (IC) chip size to acquire faster, more efficient devices (*1*). Because of the unswerving pursuit of scaling close to its physical limit and different directions of efforts (More than Moore), the integrated smart electronics can give new opportunities to the development of semiconductor technology (*2*). With More than Moore, the value of electronics is provided by integrating multiple functionalities into a single chip, which does not necessarily scale according to "Moore's law." Under this circumstance, the functionality of CMOS is not limited to acting as logic switches. By expanding the application to sensing targets, these electronics show great potential in wearable or portable scenarios such as healthcare, environmental control, and safety monitoring (*3*–*6*). What is more, with the reduction of device thickness to convert the traditional rigid semiconductors into bendable or flexible ones, these electronics exhibit more flexibility in satisfying the diverse scenes of Internet of Things applications (*7*, *8*). To realize these advances of More than Moore, integration of different functional ultrathin components with wafer-compatible process is one of the central tasks. The sensing module, due to its ability to convert different physical and chemical stimuli into electrical signals, is the core component for most smart electronics (*9*). In the field of analysis and testing, stimuli-responsive manufactures based on plasmonic structures, gaschromic materials, or metastable constructions attract considerable attention due to their portability and low cost (*10*–*14*). Nevertheless, the need for spectrometers or color charts for the comparison is inconvenient for integrated and intelligent applications. In this case, systems with a combination of stimuli-responsive materials and optoelectronic devices bring new light to the integrated sensing applications (*15*), which could bring the seamless integration of smart sensing materials with Si CMOS-compatible flexible phototransistors. The change of optical characters in sensitive materials and structures can be converted into electrical signals directly. Limited by traditional strategy for nanoscale device construction, multifunctional, flexible, and on-chip integratable characters in a single chip are supposed to be realized on demand.

Here, we report flexible silicon nanomembrane (Si-NM) phototransistors flipped with stimuli-responsive materials for multifunctional sensing through a wafer-compatible strategy (*16*). In this strategy, we fabricate flexible Si-NM sensors directly on silicon-on-insulator (SOI) wafer and release the whole Si-NM functional devices with a bottom-up thinning process. The device-first character is easy to realize large-area nanomembrane devices and makes this strategy compatible with any high-temperature budgets in the state-of-the-art process, which could be a great challenge for the traditional device-last approaches (*17*). Benefiting from this strategy, we realize flexible phototransistors with an ultrahigh on-off ratio over 10^6 for a high sensitivity. We demonstrate the functional expansibility for different sensing targets by decorating the top surface of the phototransistor with certain stimuli-responsive films. The expansibility of such on-chip Si-NM CMOS system exhibits great potential for the next-generation smart electronics interacting with the outside world for the trend of More than Moore.

RESULTS

The integratable character of the multifunctional smart sensor here benefits from a device-first, bottom-up process, which is compatible to wafer-scale fabrication of the on-chip system with state-of-the-art IC technique (*18*). Figure 1A exhibits the multilayer configuration of a typical smart sensor array. Normally, this system contains four function modules. A thin layer of smart material on top of the sensor interacts with target molecules. The constituents of this layer change according to the molecules to be detected (e.g., gas chromic materials). A ~2-μm-thick thermal silicon oxide serves as an encapsulation to

[1]Department of Materials Science, State Key Laboratory of ASIC and Systems, Fudan University, Shanghai 200433, P. R. China. [2]Shanghai Institute of Microsystem and Information Technology, Chinese Academy of Sciences, Shanghai 200050, P. R. China. [3]Center for Bio-Integrated Electronics, Northwestern University, Evanston, IL 60208, USA. [4]Department of Electrical and Electronic Engineering, Yonsei University, Seoul 03722, South Korea. [5]Department of Physics, Fudan University, Shanghai 200433, P. R. China.
*These authors contributed equally to this work.
†Corresponding author. Email: yfm@fudan.edu.cn

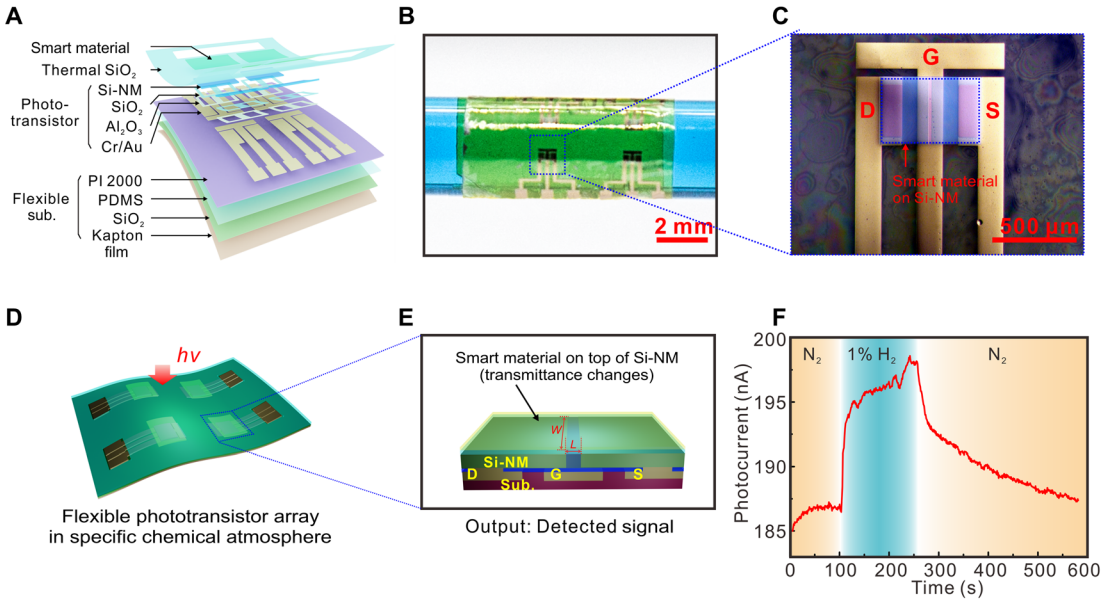

Fig. 1. Structure and basic fundamental. (**A**) Schematic illustration of key functional layers of the smart sensor based on Si-NM in an exploded view. (**B**) Photograph of the fabricated smart sensor array. (**C**) Optical image of the sensitive area of the smart sensor. S, source; D, drain; G, gate. (**D**) Schematic illustration of the smart sensor array under illumination. (**E**) Schematic illustration of the mechanism in molecule detection. (**F**) Time-dependent performance of the smart sensor in hydrogen detection. Photo credits: Gongjin Li (Fudan University).

the phototransistor below. The phototransistor could perceive the optical variations of the smart material layer and output electrical signals. To realize the high sensitivity and flexibility, a 340-nm-thick p-type Si-NM with phosphorous doping (~10^{19} cm^{-3}) or n-type with boron doping (~10^{19} cm^{-3}) at drain and source regions works as the active region of the MOSFET (metal-oxide-semiconductor field-effect transistor)-type phototransistor. The phototransistor's gate dielectric stack consists of 70-nm-thick silicon oxide (chemical vapor deposition) and 13-nm-thick aluminum oxide [atomic layer deposition (ALD)]. Electron beam–deposited Cr/Au electrodes (5/100 nm) below also act as a back reflector to enhance light absorption in the Si-NM layer. The flexible substrate consists of a spin-coated polyimide stress buffer (PI 2000, ~5 μm), a spin-coated polydimethylsiloxane (PDMS) adhesion layer (~5 μm), a sputtered silicon oxide interlayer (30 nm), and a 12.5-μm-thick Kapton film support layer.

Figure 1 (B and C) displays the optical images of a piece of the flexible sensor array and local functional region of one sensor. The curved device array on glass tube (d = 4 mm) shows outstanding flexibility (Fig. 1B). The channel length and width of the phototransistor are 20 and 400 μm, respectively (Fig. 1C). The smart material covers the Si-NM region of the phototransistor (blue dashed line region in Fig. 1C). Such a flexible sensor was achieved with a device-first, bottom-up process. Briefly, a standard semiconductor fabrication process realized the phototransistor arrays on SOI wafer directly. Then, a dry etching process removed the silicon substrate on the backside of SOI wafer. The ultrathin thickness of the whole structure substantially reduced the strain on device surface in a bent state and realized flexibility. The detailed fabrication process is introduced in Materials and Methods and fig. S1.

Figure 1 (D and E) exhibits the basic mechanism of the smart sensor. Such sensor works under certain illumination with constant intensity. When interacted with target molecules, the optical parameters of the smart material layer could change with the concentration of target molecules. The phototransistor could perceive the transmittance change of the smart material layer and transform this change into an electrical signal. As a result, the system output electrical signal, which is different from the original state and realizes optoelectronic detection of target molecules. Figure 1F displays the time-dependent performance of the smart sensor in hydrogen detection. In this circumstance, a 25-nm-thick palladium membrane serves as the gas-sensitive layer (smart material). The response and recovery time of the sensor are ~30 and ~300 s, respectively. The speed of this sensor depends on the target absorption and desorption of the sensitive material layer. More detailed characterization and analysis of the smart sensor will be discussed later.

The Si-NM photodetector is a MOSFET-type phototransistor. The metal-oxide-gate structure below the device channel has a remarkable impact on the optoelectronic response of the phototransistor. Figure 2A illustrates the gate-modulated optoelectronic characters of the device under various irradiation intensities (λ = 405 nm). The supply voltage (V_{DS}) is 0.1 V in this characterization. Without illumination, the device behaves as a typical MOSFET (more detailed characters of the transistor can be found in fig. S2). A linear extrapolation method estimated the threshold voltage (V_T) of 0.9 V (*19*). The transistor exhibits an off-state current of 3 pA and an on-state current of 35 μA. The peak effective electron mobility is ~450 cm^2 $(V{\cdot}s)^{-1}$, and the subthreshold swing is ~200 mV.

When illuminated, the drain current (I_{DS}) increases notably with irradiation intensity at a negative gate bias. The photo-to-dark current ratio could reach the degree of ~10^6 (varies with irradiation intensity). A higher photo-to-dark current ratio brings the larger distinction between output photocurrent to the noise/dark current, which is quite positive to the detection of weak signals. Three factors make major contribution to the excellent optical detectivity of the device. First, the negative gate bias remarkably restrains the dark current of the phototransistor but has limited influence to the

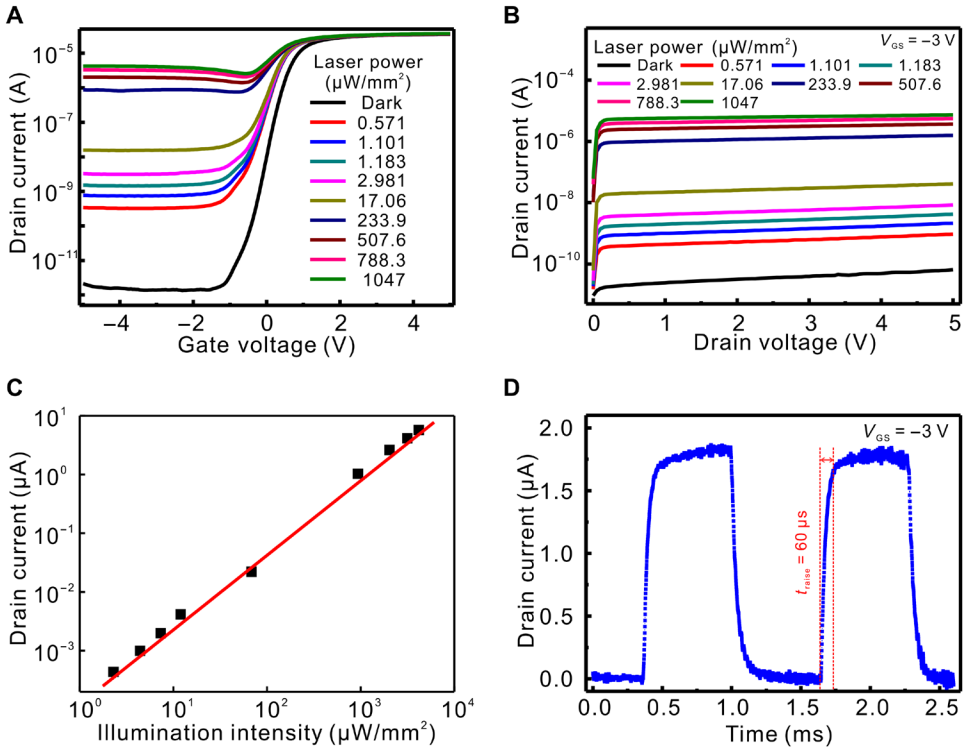

Fig. 2. Optoelectronic properties of the Si-NM phototransistor. (**A**) Drain current–gate voltage characterization under different irradiation intensity (405 nm) at a supply voltage (V_{DS}) of 0.1 V. (**B**) Drain current–drain voltage characterization under different irradiation intensity (λ = 405 nm) at a gate voltage (V_{GS}) of −3 V. (**C**) Linear response of the device at V_{DS} = 1 V and V_{GS} = −3 V. (**D**) Response time characterization of the device at V_{DS} = 1 V and V_{GS} = −3 V. The illumination power is ~0.3 mW/mm².

photocurrent. In this case, the phototransistor could achieve ultrahigh photo-to-dark current ratio at the negative gate bias, as illustrated by the I_{DS}-V_{GS} curves in Fig. 2A. This phenomenon can be explained by the variation of band structure under different gate biases (*20*). The Si-NM phototransistor here has a structure of n-type MOSFET. When a negative gate bias is applied to the light-doped p-type Si-NM channel, electrons in the channel are fully depleted, resulting in the decrease in Si-NM channel potential. The device has an n^+-p-n^+ or p^+-n-p^+ structure along the channel, which equals two p-n junctions face to face. The increased barrier height between source/drain regions to the channel markedly inhibits current leakage through the device. Under the illumination condition, the depletion region induced by gate potential promotes the separation of optically generated electron-hole pairs in the direction perpendicular to the current (*21*). Electrons can be collected by the positively biased drain region. Meanwhile, the photoexcited holes accumulate in the channel and lead to the decrease of barrier height between the channel and the drain/source region. As a result, electrons in the source become easier to inject into the channel and lead to large photocurrent gains. Second, the ultrathin thickness of the Si-NM channel makes the device more sensitive to the optical signal. On the one hand, the nanoscale thickness in the vertical direction evidently increases the light absorption per unit thickness in the light-sensitive channel (*22*). On the other hand, a thinner thickness allows efficient field-effect gate modulation; thus, the channel can be fully depleted and output extremely low dark current. For bulk devices (e.g., the channel thickness in the scale of hundred micrometers), the gate bias depletes only the channel surface and noticeable current leakage through the inner part of the bulk still remains (*23*). In addition, the gate electrode in the backside allows full exposure of the Si-NM channel to the illumination and acts as a back reflector (Fig. 1C) to further increase light absorption in the Si-NM channel.

On the basis of the discussion above, the Si-NM phototransistor operates more sensitively at negative gate bias. Figure 2B illustrates the output curves of the phototransistor at a negative gate bias (V_{GS}) of −3 V under various illumination intensities (λ = 405 nm). With the increase of drain voltage from zero bias, the drain current shoots up immediately and tends to remain constant at higher drain voltage. The saturation current grows by orders of magnitude with the increase of illumination intensity. While without gate modulation, the output current could not rise so notably (see the case of V_{GS} = 0 V in fig. S3). Under this circumstance, a positive supply voltage of V_{DS} = 1 V is enough for an efficient collection of photogenerated carriers through the channel. The ideal working bias can be set to V_{GS} = −3 V and V_{DS} = 1 V. Figure 2C demonstrates that the phototransistor could maintain good linear response with the increase of light intensity whether under weak illumination or strong irradiation as high as several milli-watts per square millimeter.

Figure 2D exhibits the optoelectronic response of the Si-NM phototransistor as a function of time. The phototransistor takes ~60 μs to rise to a stationary state and ~120 μs to decay to the original state in the optical transient response tests. These values indicate that the response speed is comparable to commercial phototransistors (*24*). The high carrier mobility in the single-crystal Si-NM channel and the small channel length (*L* in Fig. 1C) contribute to the efficient collection of photogenerated carriers, reducing the transit time of carriers through the channel. In conclusion, the ultrahigh photo-to-dark current ratio and linear output characters are quite

positive to the optoelectronic detection of various physical/chemical signals, while the fast speed of the phototransistor allows the system to respond immediately to the external stimulus.

One of the most remarkable challenges for inorganic semiconductors in flexible optoelectronic applications is the reduction of strain in the bent state. Normally, the maximum ε locates in the region farthest from the neutral surface of a bent structure. Under these circumstances, the critical bending radius r_c of the Si-NM–based smart sensor can be estimated as (*25*)

$$r_c = \frac{t}{2\varepsilon_{failure}} \quad (1)$$

where t is the total thickness of the device and $\varepsilon_{failure}$ is the fracture limit. The middle layer of the device was taken as the neutral surface in this estimation. For Si-NM on top of the device surface, $\varepsilon_{failure}$ is ~1% (*26*). The total thickness of the device is ~20 μm. In this circumstance, the theoretical bending limit of the flexible sensor is ~1 mm. What is more, the polyimide substrate was regarded as a rigid material in the estimation above. In practical terms, the soft polymer substrate could share some of the bending stress by means of elastic deformation. In that case, the limited bending radius $\varepsilon_{failure}$ of our device has the opportunity to be smaller than 1 mm in practice.

To affirm the bend resistance of the smart sensor, we carried out mechanical bending tests. Figure 3A exhibits the Si-NM phototransistor's responsivity as a function of bending cycles to a 7-mm bend radius. The inset exhibits the device array in the bending state. The responsivities (R) were calculated with the following equation

$$R = \frac{I}{PA} \quad (2)$$

where I is the output current of the device that corresponds to the performance after certain loops of bending, P is the illumination intensity in the characterization (1.04 mW/mm^2), and A is the area of light-sensitive channel of the device (20 μm × 400 μm). The gate bias was set to V_{GS} = −3 V, and the supply voltage was set to V_{DS} = 1 V. The responsivity maintains at a high level of 0.89 A/W throughout the characterization. This indicates that no functional damage occurs during the cyclic bending tests. In Fig. 3B, the highly overlapped curves demonstrate the resistance of the device to the bending strain. The corresponding output curves (I_{DS}-V_{DS} at V_{GS} = −3 V) and transfer curves (I_{DS}-V_{GS} at V_{DS} = 0.1 V) under illumination (1.04 mW/mm^2) were also provided in fig. S4. All these stable performances after bending cycles verify the good stability of this smart sensor in flexible applications. The bending compatibility of the smart sensor markedly expands the application range in, e.g., narrow space and tubular structures for gas and chemical component detection.

The high performance of the Si-NM phototransistor makes it an ideal platform for the optoelectronic detection of various specific molecules. A typical example is the optoelectronic sensing of hydrogen concentration in the atmosphere. Hydrogen is widely used in today's industrial manufacturing and shows great potential as a future green energy resource. The flammable and explosive characters of hydrogen require that the possible leakage should be detected promptly before any catastrophic event occurs (*27*). According to the above scenario, various H_2 gas sensors have been developed. Their working mechanisms can mainly be classified as electric signal variation, color change, and visible structure transformation.

As a necessary supplement, the optoelectronic gas sensing here gives an opportunity to avoid any direct contact between flammable

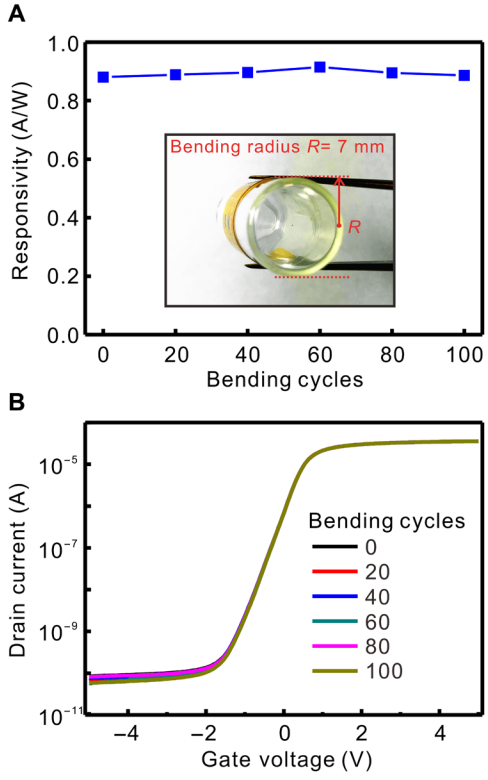

Fig. 3. Bend resistance of the phototransistor. (**A**) The responsivity of the device after various bending cycles (V_{GS} = −3 V and V_{DS} = 0.1 V). Inset exhibits the bending state of the device in the test. Photo credit: Gongjin Li (Fudan University). (**B**) Electronic characters of the phototransistor (in dark) after various bending cycles (V_{GS} = −3 V and V_{DS} = 0.1 V).

H_2 gas and conductive path of the device. The structure of the smart sensor for the H_2 detecting application can be found in fig. S5. A thin layer (~25 nm) of palladium (Pd) nanomembrane deposited on PE (polyethylene) film was arranged on the top surface of the Si-NM light-sensitive area. Previous studies have shown that the optical properties of Pd film could change remarkably by means of hydrogen insertion (*28*). When interacted with hydrogen, the optical parameter changing the Pd nanomembrane could be detected immediately by the Si-NM phototransistor below. In that case, the concentration information could be output with the electrical signal by the smart sensor. Figure 4A exhibits the hydrogen sensing performance of the smart sensor, and the inset shows the photo of the characterization configuration. A plastic container sealed with polyethylene film provides an airtight environment for the hydrogen concentration characterization. The gas inlet and outlet were placed through the side wall of the chamber face to face. A λ = 405-nm laser with a constant intensity of ~0.8 mW/mm^2 irradiates the smart sensor. The hydrogen gas was mixed with high-purity nitrogen with a certain ratio to realize different H_2 volume concentrations. The mixed gas was injected into the chamber with a flow rate of 0.2 liter/min and steady for 3 min for the characterization. The I_{DS}-V_{GS} curves in Fig. 4A exhibits that the photocurrent rises with the increase of H_2 concentration. The sensor shows much more discrimination to the change of H_2 concentration at a negative gate bias, which benefits from the gate-modulated high sensitivity of the phototransistor (already discussed above). Figure 4B demonstrates the detectivity of the smart optoelectronic gas sensor at a

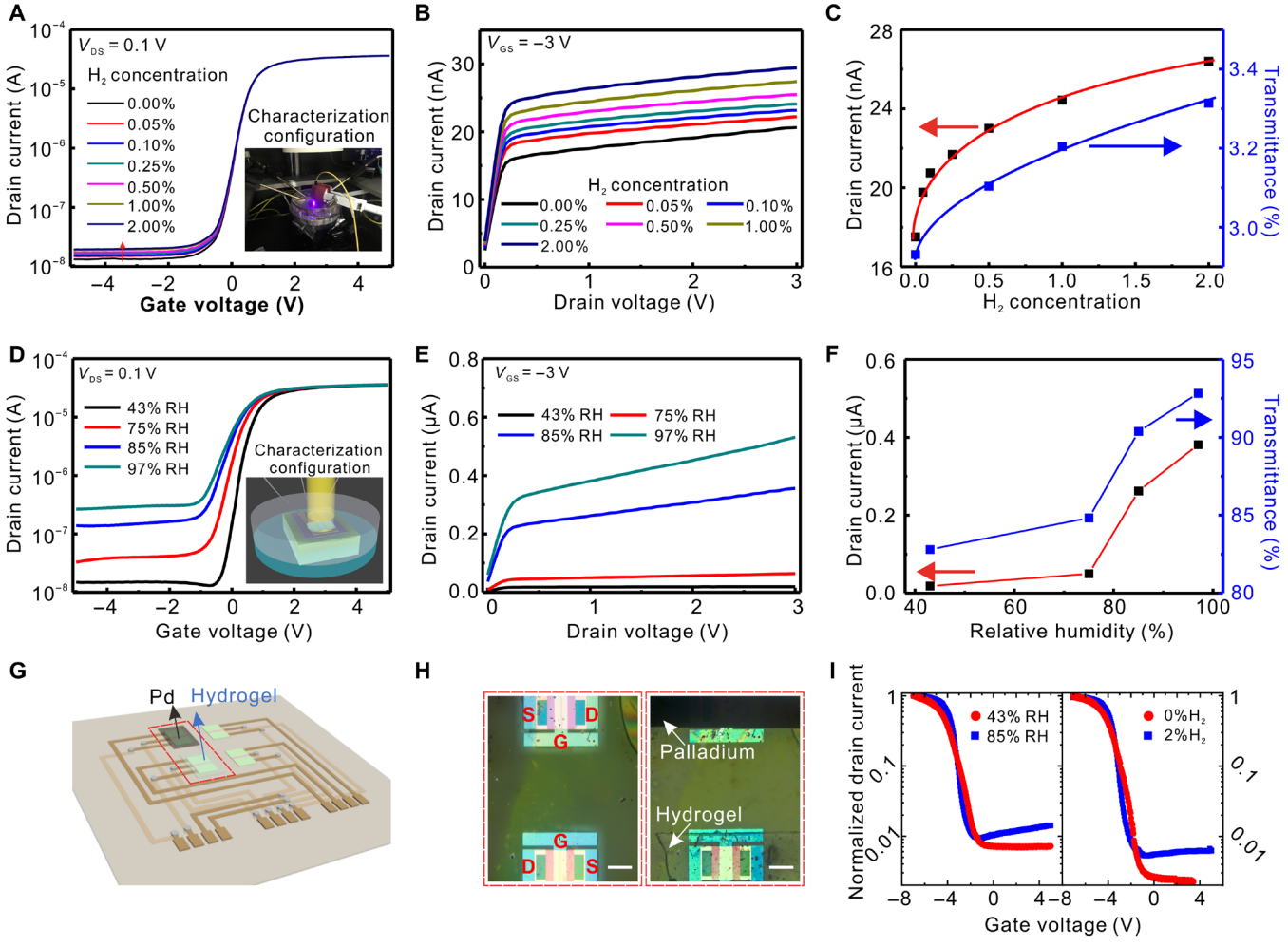

Fig. 4. Performance of the smart sensor in the detection of hydrogen concentration and humidity measurement. (**A**) Transfer curves of the device at various hydrogen concentrations. The inset shows the characterization configuration in the experiment. The supply voltage V_{DS} = 0.1 V. The intensity of 405-nm laser is ~0.8 mW/mm^2. (**B**) Output curves of the smart sensor at various hydrogen concentrations. The gate bias V_{GS} = −3 V. (**C**) Variation trend of the output signal (black squares; V_{GS} = −3 V and V_{DS} = 1 V) and transmittance of the Pd film (blue squares) with the increase of H_2 concentration. (**D**) Transfer curves of the device at various relative humidities. The inset shows the characterization configuration in the experiment. The supply voltage V_{DS} = 0.1 V. The intensity of 405-nm laser is ~0.8 mW/mm^2. (**E**) Output curves of the smart sensor at various relative humidities. The gate bias V_{GS} = −3 V. (**F**) Variation trend of the output signal (black squares; V_{GS} = −3 V and V_{DS} = 1 V) and transmittance of the hydrogel film (blue squares) with the increase of relative humidity. (**G**) Schematic illustration of the dual-channel sensing array on a single chip. The deep color film covered on the light-sensitive area is palladium, while the almost transparent one is hydrogel. (**H**) Optical image of the light-sensitive area (left) and (right) covered by both palladium and hydrogel smart materials. The upper and dark one is palladium membrane, and the lower and transparent one is the hydrogel film. Scale bars, 300 μm. (**I**) Drain current–gate voltage performance under different hydrogen condition (left) and relative humidity (right). Photo credits: Gongjin Li (Fudan University).

negative gate bias of −3 V. The output current signal shows great discrimination at different H_2 concentrations. A low H_2 concentration of 0.05 volume percent (volume %) has been detected (see red line in Fig. 4B), and the detection of a much lower H_2 concentration is also possible because of the distinction between 0.05 volume % H_2 and 0.00 volume % H_2. This detectivity is comparable to the reported high-performance electric H_2 sensors and much better than recent visual H_2 sensors (*29*). In addition, considering that the standby current is in the magnitude of tens of picoampere and the working current is below 30 nA, the power consumption of this detecting module could be below the magnitude of microwatt. The ultralow-power consumption is another superiority of this multifunctional sensor.

Figure 4C records the variation trend of the output signal (drain current, black squares, V_{GS} = −3 V and V_{DS} = 1 V) with the increase of H_2 concentration. The transmittance variation of palladium membrane of the same thickness was also measured with a ultraviolet (UV)–visible spectrometer for reference (λ = 405 nm; blue squares in Fig. 4D). Continuous transmittance spectrum is provided in fig. S6. The transmittance shows the same increased tendency in the whole spectrum range of investigation (350 to 750 nm). Both the output current and transmittance rise obviously at the beginning and tend to slow down at higher H_2 concentration. This output current variation corresponds with the palladium membrane's optical parameter. During the exposures to hydrogen, there is an increase in the transmittance (T) of palladium membrane and a decrease in the reflectance (R) (*30*)

$$T \approx \frac{16\, n_s (n^2 + k^2)}{[(n + n_s)^2 + k^2]} \exp(-4\pi kd/\lambda) \qquad (3)$$

$$R \approx \frac{(1-n)^2 + k^2}{(1+n)^2 + k^2} \quad (4)$$

where n and k are the real part and imaginary part of palladium membrane's refractive index at wavelength λ, respectively. In these equations, d is the thickness of palladium membrane and n_s is the refractive index of the substrate below palladium membrane. According to the equations above, both R and T variation link to the decrease in the imaginary part of the refractive index (k), also known as extinction coefficient. In particular, the change of k and membrane thickness d could markedly influence the transmittance T because of the exponential dependence of transmittance on the extinction coefficient and transmittance.

During the exposure to hydrogen, the palladium nanomembrane absorbs H atoms immediately. The insertion of H atoms in palladium lattice structure leads to more semiconductor behavior of hydrided palladium (Pd:H) than pure palladium and changes of optical permittivity (*31*). These changes can be explained by the impurity scattering effect by hydrogen in palladium (*30*). The imaginary part ε_2 of optical permittivity relates to the refractive index in Eq. 1 by

$$\varepsilon_2 = 2nk \quad (5)$$

and the optical resistivity ρ by

$$\varepsilon_2 = \frac{1}{\omega\rho} \quad (6)$$

where ω is the angular frequency of the irradiation field. The impurity scattering by hydrogen atoms in palladium induces the increase of optical resistivity ρ, which means the decrease of nk. Previous measurement shows that the real part of the refractive index n always increases in hydrogen-exposed palladium membranes in the spectrum range of 275 to 600 nm (*32*). In that case, the extinction coefficient k decreases much more remarkably than the increase of n to guarantee a decreased product of nk during hydrogen exposure. Taking Eqs. 1 and 2 into consideration, the reduced k contributes to the total optical transmittance increase through the palladium nanomembrane, thus enhancing the output (drain current) of the experiment results in Fig. 4C.

The variation of thickness d is another important factor that influences the total transmittance of the palladium nanomembrane. In hydrogen ambient, the hydrogen atoms insert into palladium nanomembrane with two principal mechanisms (*33*). At the beginning with a low H_2 concentration, H atoms enter the interstitial void and preexisting microstructural defects such as vacancies, grain boundaries, and dislocations of palladium film (*34*). In this case, the influence to the thickness d is negligible. When hydrogen atoms occupy the interstitial sites of palladium film with further increase of hydrogen concentration, a phase transition from α- to β-phase happens in palladium film (*35*). Large amounts of H atoms diffuse into the film, breaking the bonds of palladium structure and leading to a notable deformation in the film. According to Eq. 1, the increase of thickness d reduces the total transmittance T. This influence competes with the extinction coefficient k discussed above. As a result, the increase of total transmittance tends to slow down at larger H_2 concentration. In this circumstance, the measured output current and transmittance in Fig. 4C tends to slow down at larger H_2 concentration. The insertion and desertion time of H atoms in palladium nanomembrane dominates the response speed of the smart sensor. That is why the device needs tens of seconds to respond to the hydrogen stimulus in Fig. 1E. It should also be noted that there is a little difference between the relative growth of output current and the transmittance results in Fig. 4C. This is mainly due to the different substrate refractive index n_s (Eq. 1) in the optoelectronic gas sensing (Si-NM phototransistor as the substrate) and UV-visible spectrum characterization (quartz glass as the substrate).

Optoelectronic hydrogen sensing above is just one application instance. The diversity of specific sensitive materials for different stimuli provides alternatives for the optoelectronic detection of various physical or chemical signals in ambient. Here, the optoelectronic humidity sensing by the smart sensor is also exhibited to demonstrate expansibility of this system. Currently, a reliable monitoring and controlling of moisture are highly in demand in various environments because even trace amounts of water molecules can markedly influence the reliability and functionality of materials and systems (*36*). The on-chip humidity sensing benefits the integration and miniaturization of the flexible electronic circuit system. The structure of the smart sensor for the humidity sensing application can be found in fig. S7. A thin layer (~20 μm) of hydrogel film (UV-cured hydroxyethyl methacrylate–acrylic acid copolymer) was chosen as the smart sensitive material and stick on the top surface of the Si-NM light-sensitive area. A thin layer of compact aluminum oxide (Al_2O_3) was deposited on the thermal silicon oxide (SiO_2) to enhance the encapsulation in moisture ambient. The remaining structures are the same with the hydrogen sensor discussed above.

Figure 4D exhibits the optoelectronic performance of the smart sensor with the gate voltage under various relative humidities (RHs), which indicates that the photocurrent in reverse cutoff region rises substantially with the increase of RH. The inset shows the experimental configuration of the optoelectronic humidity sensing system. A plastic container sealed with polyethylene film provides an airtight environment for the humidity characterization. The alterable RH was acquired by injecting and extracting saturated salt solutions (K_2CO_3, NaCl, KCl, and K_2SO_4) with an injector through the polyethylene film. The corresponding RH values are 43, 75, 85, and 97%, respectively. The device was placed on a dais in the plastic container. A λ = 405-nm laser with a constant intensity of ~68 μW/mm^2 irradiates the smart sensor. All characterizations were carried out after a 10-min stabilization in constant humidity ambient. Figure 4E illustrates the detectivity of the smart optoelectronic humidity sensor (I_{DS}-V_{DS}) at a negative gate bias of −3 V. With the rising of drain voltage (V_{DS}) from zero, the output current (I_{DS}) exhibits a sharp linear increase at the beginning and a flat growth at higher drain voltage. The inflection point is nearly 0.2 V, corresponding to the minimum supply voltage needed for an efficient collection of photogenerated carriers in the channel of the smart sensor. The rising of photocurrent with drain voltage is a little different compared with the case of optoelectronic sensing of hydrogen concentration. This indicates that other extra effects may exist in the optoelectronic detection of RH with the smart sensor.

For the further study of the mechanism in the optoelectronic humidity sensor, the variation trend of the output signal (drain current) at the optimum working condition (V_{GS} = −3 V and V_{DS} = 1 V) was recorded as black squares in Fig. 4F. The output current increases slightly in the low humidity range and becomes sharp over 75% RH, exhibiting similar tendency with the change of hydrogel film's transmittance (λ = 405 nm) at various humidities. The transmittance of the hydrogel film in the spectrum range of 350 to 750 nm at various humid atmospheres was also provided in fig. S8. In all the measured

spectrum range, the transmittance shows consistent tendency, which is the same with that under λ = 405-nm illumination. This phenomenon corresponds with the relationship between hydrogel transmittance and water content in the previous study (*37*).

Absorbing water from the surrounding environment is a primary property of hydrogel. In general, the absorbed water in methacrylate-based hydrogel can be categorized into two types: free water and bound water (*38*). Both contribute to the equilibrium water content of the hydrogel. It is known that porous materials are expected to scatter light in some degree, resulting in lower optical transmittance. As polymer materials, defects or pores between polymer chains of hydrogel inevitably lead to light scattering at air-polymer interfaces. Because of the similar optical properties of water and hydrogel molecules, filling this air space with water could improve the total transparency. Previous research also demonstrated that hydrogel absorbs much more water in the high humid atmosphere, indicating that the water content in hydrogel does not increase linearly with ambient humidity (*39*). That is the reason why hydrogel's transmittance shows a nonlinear relationship with the RH in Fig. 4F. It should also be noted that with the rising of RH, the increased ratio of the output current is higher than that of transmittance. Two factors contribute to this phenomenon: On prolonged exposure to high humid ambient, the swelled hydrogel becomes much softer and sticks more tightly on the surface of the Si-NM phototransistor, which further reduces adverse light scattering through the interfaces. Another reason is that the existence of hydrogel notably increases water molecules on the device surface. The moist surface could provide a channel for charge transportation (*40*). This phenomenon is only obvious when the device is under illumination. There is also a slight increase of dark current in the Si-NM phototransistor in a high humid atmosphere (fig. S9). But the contribution to the total current is below 0.1 nA even in high humid atmosphere, which is less than 1‰ of the increased photocurrent in the same humid atmosphere under illumination. The sensor is much more sensitive for humidity detection under illumination.

Humidity- and hydrogen-responsive materials can be both integrated on one device to demonstrate the capability of multimodal sensing. As shown in the schematic illustration (Fig. 4G), Pd/hydrogel films covered individual phototransistors and the electrode patterns were rescheduled to facilitate the measurements. Figure 4H shows optical image of two phototransistors before and after the smart material integration. The deep color film covered on the light-sensitive area was palladium, while the nearly transparent one was hydrogel. With two types of smart materials, two-channel sensing was carried out and the performance of both sensors is presented in Fig. 4I. The left panel illustrates the transfer property of the humidity sensor under different humidities (RH = 43 and 85%), and the right panel depicts the case of the hydrogen sensor with 0 and 2% H_2 concentration. Each sensor's subthreshold current underwent an obvious change when different stimuli were introduced. As discussed above, both hydrogen-absorbed palladium and the water-saturated hydrogel achieved a higher optical transmittance, thus resulting in a higher

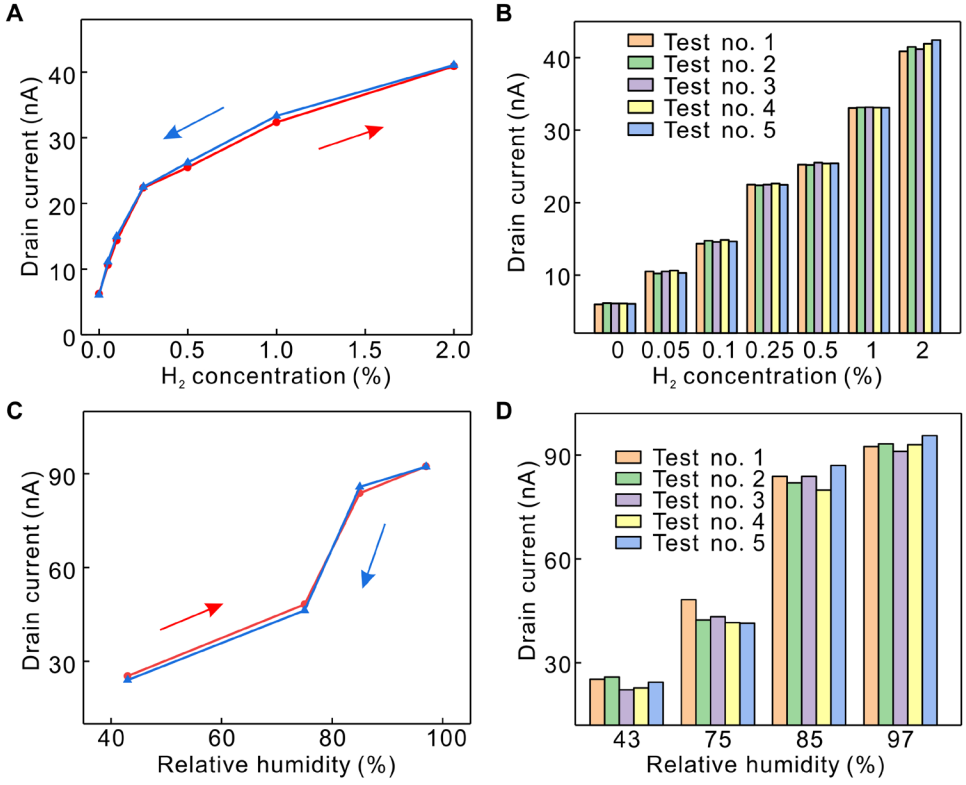

Fig. 5. Repeatability of relative humidity optoelectronic hydrogen concentration and relative humidity sensing capability. (**A**) Hydrogen sensing from low to high concentrations and then from high to low concentrations. The red line presents the low-to-high process, while the blue line presents the high-to-low process. (**B**) Multi-time tests of H_2 concentration sensing. (**C**) Humidity measurement from low to high concentrations and then from high to low concentrations. The red line presents the low-to-high process, while the blue line presents the high-to-low process. (**D**) Multi-time tests of humidity sensing.

light-triggered subthreshold current. As long as the array size and the varieties of smart materials integrated increase, we could expand the two-channel system to various types of sensing functions.

To verify the reliability to external stimuli of this smart sensor, cyclic characterization and statistical tests were carried out under various hydrogen or humidity concentrations. Figure 5A records the variation trend of the output signal [drain current, $V_{GS} = 1$ V, $V_{DS} = 0.1$ V, PMOS (p-type metal oxide semiconductor)] with the variation of H_2 concentration. For each hydrogen level, the device exhibits a stable signal value in the process of increased or decreased gas concentration. Certainly, the repeatability is in expectation. Figure 5B illustrates the signal strength in five independent tests. The device responds in a quite similar level at different H_2 concentrations. In the detection of RH, the reliability of the smart sensor was demonstrated analogously. Figure 5C records the output signal corresponding with different humidities in cyclic experiment, while Fig. 5D displays the coincident responsibility in five independent tests. All these data determine the reliability to different types of stimuli. The Si-NM–based smart sensor exhibits great potential in practical application as a multifunctional detector.

DISCUSSION

The optoelectronic sensing of hydrogen concentration and environment humidity demonstrate the functional expandability of the smart sensor. This flexible device is more like an expandable low-power working platform, and various molecular analyses and sensing can be realized by decorating the top surface of the phototransistor with different sensitive materials. Figure 6A illustrates the integrated system design and the concept for the smart digital dust. Benefiting from the device-first process, standard logical and power units as well as Si-NM phototransistor array (detecting units and blank reference) can be integrated on one flexible chip with standard IC technique. Figure 6B is the schematic illustration of the complete system we fabricated by integrating our sensors with amplifier and power supply on a substrate to demonstrate the feasibility of our idea. The real-time sensing of humidity and processing is achieved, as shown in movie S1. The current output in Fig. 6C and the program flow chart in Fig. 6D exhibit the mechanism of this system. On the standby mode, the sensor and blank reference output current signal I_0 and I_A. The proportionality, $\alpha = I_A/I_0$, maintains below a certain threshold value (k) without target stimulus. When interacted with target gas (e.g., hydrogen), the transmittance change of the sensitive material above sensor A leads to an increase of I_A (blue curve in Fig. 6C), while the current output of the reference sensor remains in the original state (red curve in Fig. 6C). By fitting the α value with prestored data, the system output the exact value of stimulus level in the form of digital signals. Benefits from the blank reference in the system, the smart sensor could operate regardless of external illumination intensity. With a similar principle, various detecting units could be integrated into one flexible chip. In that case, the flexible

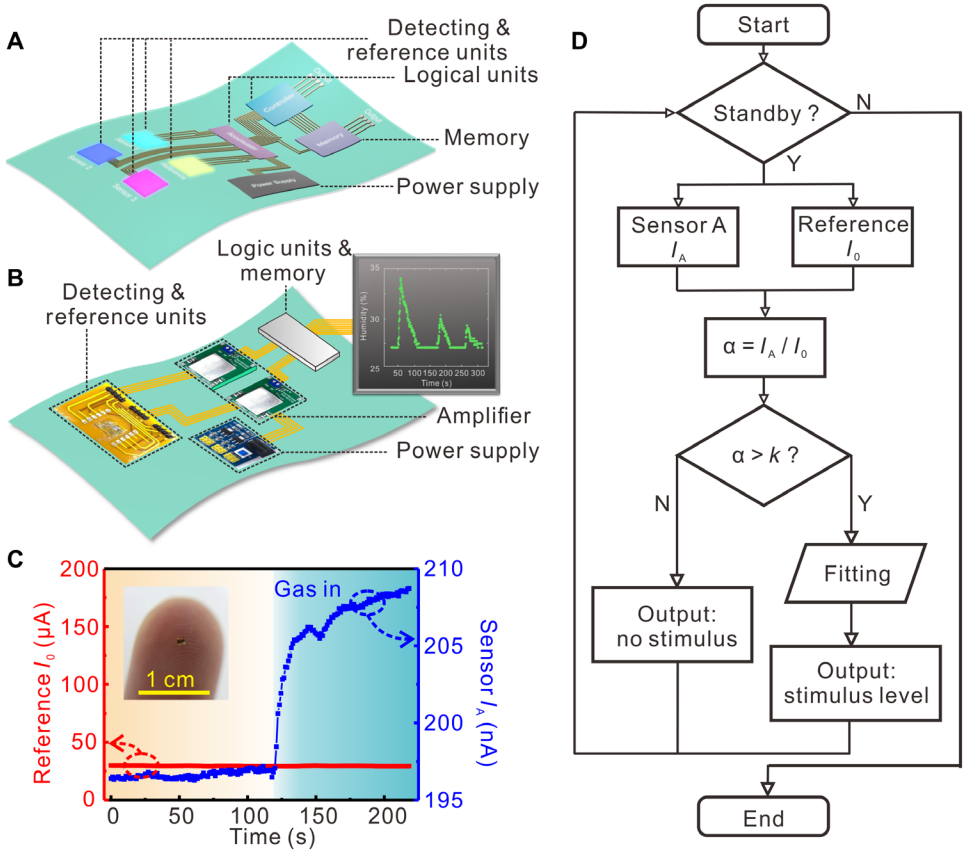

Fig. 6. Integrated system design. (**A**) Functional modules on the flexible smart system. (**B**) Complete system composed of the phototransistor array (optical image), amplifier, power supply, and logic units/memory for the humidity test in real time. (**C**) Time-dependent current output of the reference sensor (blank phototransistor; red dashed lines) and H_2 sensor (blue dashed lines). Photo credit: Chunyu You (Fudan University). (**D**) Program flow chart of the smart system.

and integrated multifunctional detection system can be realized. Besides single isolated phototransistors, we took a step forward to construct an active matrix-type device (four columns and four rows) with a vanadium dioxide (VO_2) film to realize heating mapping as an enhanced function (fig. S10). VO_2 film undergoes a metal-insulator transition near room temperature (~68°C), leading to transmittance variation, thus influencing the subthreshold drain current of the phototransistor. A 1550-nm infrared laser was shed on the device, a hard mask was used to create distinctive heating region on our device, and the heating map can be achieved correctly.

The optoelectronic sensing of external stimuli brings new light to the field of analysis and testing. A combination of high-performance phototransistors and stimuli-responsive materials demonstrates the functional expandability of Si-NM devices in the detection of various physicochemical stimuli. The optoelectronic sensing of hydrogen concentration below 0.05 volume % and RH from 43 to 97% has been realized. Theoretical analysis and comparative experiments reveal the mechanism of hydrogen and humidity detection. The device-first, wafer-compatible fabrication of the flexible smart sensor based on Si-NM indicates the convenience for the integration of different sensing and control components to meet multifunctional requirements on one single chip, which is promising for the smart digital dust application. We believe that achievements in this work suggest a promising future for the next-generation More than Moore technologies.

MATERIALS AND METHODS

The SOI wafers were purchased from the Shanghai Simgui Technology Co. Ltd. The PI 2000 and Kapton film were purchased from DuPont Co. Ltd. Other reagents were purchased from Sinopharm Chemical Reagent Co. Ltd.

Fabrication of Si-NM phototransistor

Steps 1 and 2 in fig. S1 illustrate the fabrication of the Si-NM phototransistor on rigid wafer. The process of Si-NM phototransition starts from the back-grinding of an SOI wafer (340-nm-thick device Si and 2-μm-thick buried thermal SiO_2, weakly p-doped/n-doped) to reduce the wafer thickness from ~670 to 200 μm. Standard RCA cleaning removes contamination on wafer surface. A 600-nm-thick SiO_2 doping mask is then formed by the plasma-enhanced chemical vapor deposition (PECVD), followed by photolithography and chemical etching. The active region of the phototransistor is doped by the liquid source phosphorus oxychloride and defined by reactive ion etching (RIE). The gate dielectric layer consists of 70-nm SiO_2 and 13-nm Al_2O_3, deposited by PECVD and ALD, respectively. Cr/Au (5/100 nm) electrodes are deposited by the electron beam evaporation. At last, rapid thermal annealing at 350°C activated metal contacts and completed the fabrication of the Si-NM phototransistor on rigid wafer.

Thinning process

Steps 3 and 4 in fig. S1 illustrate the thinning process to get the flexible phototransistors from the rigid SOI wafer. A uniform coating and curing process of polyimide (PI 2000) acts as a stress buffer and protects the device surface. A 12.5-μm-thick Kapton film acts as the flexible handling substrate. An ultrathin layer of spin-coated PDMS (~5 μm) bonded the Kapton film and device together. After a curing process in a vacuum oven for 40 min at 110°C, the whole structure face down stack on a temporary glass substrate with ~10-μm cured PDMS as a soft adhesive, leaving the back silicon substrate exposed. Then, inductively coupled plasma RIE (SF_6/O_2) removed the 200-μm-thick silicon substrate away. The buried oxide layer in SOI acts as an etching barrier because of the high selectivity of SF_6 in the dry etching process. At last, the contact window is defined by photolithograph and opened by etching of SiO_2. Peeling the manufacture above the Kapton film from the temporary glass substrate yields the final Si-NM phototransistor.

Decorating Si-NM phototransistor surface with sensitive materials

Steps 5-1 and 5-2 in fig. S1 illustrate the realization of the optoelectronic sensor for hydrogen sensing and humidity measurement, respectively. For the application of optoelectronic sensing of hydrogen concentration, a palladium layer of 25 nm is deposited on an ultrathin polyethylene film, and the film is then stuck on the light-sensitive channel of the Si-NM phototransistor. For the application of humidity measurement, a 10-nm-thick Al_2O_3 layer was predeposited with ALD to protect the circuit of the Si-NM phototransistor in moist environment. After that, a thin layer (~20 μm) of hydrogel film (UV-cured hydroxyethyl methacrylate–acrylic acid copolymer) is decorated on the light-sensitive channel of the Si-NM phototransistor.

SUPPLEMENTARY MATERIALS

Supplementary material for this article is available at http://advances.sciencemag.org/cgi/content/full/6/18/eaaz6511/DC1

REFERENCES AND NOTES

1. M. A. Yoder, Z. Yan, M. Han, J. A. Rogers, R. G. Nuzzo, Semiconductor nanomembrane materials for high-performance soft electronic devices. *J. Am. Chem. Soc.* **140**, 9001–9019 (2018).
2. M. M. Waldrop, The chips are down for Moore's law. *Nature* **530**, 144–148 (2016).
3. J. Li, E. Song, C.-H. Chiang, K. J. Yu, J. Koo, Y. Du, Y. Zhong, M. Hill, C. Wang, J. Zhang, Y. Chen, L. Tian, Y. Zhong, G. Fang, J. Viventi, J. A. Rogers, Conductively coupled flexible silicon electronic systems for chronic neural electrophysiology. *Proc. Natl. Acad. Sci. U.S.A.* **115**, E9542–E9549 (2018).
4. M. Cho, J. Yun, D. Kwon, K. Kim, I. Park, High-sensitivity and low-power flexible schottky hydrogen sensor based on silicon nanomembrane. *ACS Appl. Mater. Interfaces* **10**, 12870–12877 (2018).
5. Q. Guo, Z. Di, M. G. Lagally, Y. Mei, Strain engineering and mechanical assembly of silicon/germanium nanomembranes. *Mater. Sci. Eng. R Rep.* **128**, 1–31 (2018).
6. K. Zhang, Y. H. Jung, S. Mikael, J.-H. Seo, M. Kim, H. Mi, H. Zhou, Z. Xia, W. Zhou, S. Gong, Z. Ma, Origami silicon optoelectronics for hemispherical electronic eye systems. *Nat. Commun.* **8**, 1782 (2017).
7. D.-Y. Khang, H. Jiang, Y. Huang, J. A. Rogers, A stretchable form of single-crystal silicon for high-performance electronics on rubber substrates. *Science* **311**, 208–212 (2006).
8. H. Fang, K. J. Yu, C. Gloschat, Z. Yang, C.-H. Chiang, J. Zhao, S. M. Won, S. Xu, M. Trumpis, Y. Zhong, E. Song, S. W. Han, Y. Xue, D. Xu, G. Cauwenberghs, M. Kay, Y. Huang, J. Viventi, I. R. Efimov, J. A. Rogers, Capacitively coupled arrays of multiplexed flexible silicon transistors for long-term cardiac electrophysiology. *Nat. Biomed. Eng.* **1**, 0038 (2017).
9. S. R. Madhvapathy, Y. Ma, M. Patel, S. Krishnan, C. Wei, Y. Li, S. Xu, X. Feng, Y. Huang, J. A. Rogers, Epidermal electronic systems for measuring the thermal properties of human skin at depths of up to several millimeters. *Adv. Funct. Mater.* **28**, 1802083 (2018).
10. L. Tian, E. Chen, N. Gandra, A. Abbas, S. Singamaneni, Gold nanorods as plasmonic nanotransducers: Distance-dependent refractive index sensitivity. *Langmuir* **28**, 17435–17442 (2012).
11. Y.-A. Lee, S. S. Kalanur, G. Shim, J. Park, H. Seo, Highly sensitive gasochromic H_2 sensing by nano-columnar WO_3-Pd films with surface moisture. *Sens. Actuators B Chem.* **238**, 111–119 (2017).

12. J.-L. Chen, C.-C. Chang, Y.-K. Ho, C. L. Chen, C.-C. Hsu, W.-L. Jang, D.-H. Wei, C.-L. Dong, C.-W. Pao, J.-F. Lee, J.-M. Chen, J. Guo, M.-K. Wu, Behind the color switching in gasochromic VO_2. *Phys. Chem. Chem. Phys.* **17**, 3482–3489 (2015).
13. B. Xu, Z. Tian, J. Wang, H. Han, T. Lee, Y. F. Mei, Stimuli-responsive and on-chip nanomembrane micro-rolls for enhanced macroscopic visual hydrogen detection. *Sci. Adv.* **4**, eaap8203 (2018).
14. Z. Tian, B. Xu, B. Hsu, L. Stan, Z. Yang, Y. F. Mei, Reconfigurable vanadium dioxide nanomembranes and microtubes with controllable phase transition temperatures. *Nano Lett.* **18**, 3017–3023 (2018).
15. K. N. Noh, S. Il Park, R. Qazi, Z. Zou, A. D. Mickle, J. G. Grajales-Reyes, K.-I. Jang, R. W. Gereau IV, J. Xiao, J.-A. Rogers, Miniaturized, battery-free optofluidic systems with potential for wireless pharmacology and optogenetics. *Small* **14**, 1702479 (2018).
16. G. Li, E. Song, G. Huang, R. Pan, Q. Guo, F. Ma, B. Zhou, Z. Di, Y. Mei, Flexible transient phototransistors by use of wafer-compatible transferred silicon nanomembranes. *Small* **14**, 1802985 (2018).
17. A. M. Hussain, M. M. Hussain, CMOS-technology-enabled flexible and stretchable electronics for internet of everything applications. *Adv. Mater.* **28**, 4219–4249 (2016).
18. G. Li, E. Song, G. Huang, Q. Guo, F. Ma, B. Zhou, Y. Mei, High-temperature-triggered thermally degradable electronics based on flexible silicon nanomembranes. *Adv. Funct. Mater.* **28**, 1801448 (2018).
19. B. Huang, D. K. Reinhard, Electric field-dependent conductivity of polycrystalline diamond thin films. *Appl. Phys. Lett.* **59**, 1494–1496 (1991).
20. H. Yamamoto, K. Taniguchi, C. Hamaguchi, High-sensitivity SOI MOS photodetector with self-amplification. *Jpn. J. Appl. Phys.* **35**, 1382–1386 (1996).
21. W. Zhang, M. Chan, S. K. H. Fung, P. K. Ko, Performance of a CMOS compatible lateral bipolar photodetector on SOI substrate. *IEEE Electr.Device Lett.* **19**, 435–437 (1998).
22. J.-H. Seo, K. Zhang, M. Kim, D. Zhao, H. Yang, W. Zhou, Z. Ma, Flexible phototransistors based on single-crystalline silicon nanomembranes. *Adv. Opt. Mater.* **4**, 120–125 (2016).
23. D. Kufer, G. Konstantatos, Photo-FETs: Phototransistors enabled by 2D and 0D nanomaterials. *ACS Photonics.* **3**, 2197–2210 (2016).
24. V. N. Tran, R. Stuart, H. Bhavsar, *Phototransistor Switching Time Analysis* (California Eastern Laboratories, 2009).
25. J. A. Rogers, J. H. Ahn, in *Silicon Nanomembranes: Fundamental Science and Applications* (John Wiley & Sons, 2016), chap. 3.
26. L. Yan, H. B. Lu, G. T. Tan, F. Chen, Y. L. Zhou, G. Z. Yang, W. Liu, Z. H. Chen, High quality, high-*k* gate dielectric: Amorphous $LaAlO_3$ thin films grown on Si (100) without Si interfacial layer. *Appl. Phys. A.* **77**, 721–724 (2003).
27. L. Schlapbach, Technology: Hydrogen-fuelled vehicles. *Nature* **460**, 809–811 (2009).
28. K. Kalli, A. Othonos, C. Christofidès, Characterization of reflectivity inversion, α-and β-phase transitions and nanostructure formation in hydrogen activated thin Pd films on silicon based substrates. *J. Appl. Phys.* **91**, 3829–3840 (2002).
29. T.-R. Rashid, D.-T. Phan, G.-S. Chung, Effect of Ga-modified layer on flexible hydrogen sensor using ZnO nanorods decorated by Pd catalysts. *Sens. Actuators B Chem.* **193**, 869–876 (2014).
30. J. I. Avila, R. J. Matelon, R. Trabol, M. Favre, D. Lederman, U. G. Volkmann, A. L. Cabrera, Optical properties of Pd thin films exposed to hydrogen studied by transmittance and reflectance spectroscopy. *J. Appl. Phys.* **107**, 23504 (2010).
31. G. Fortunato, A. Bearzotti, C. Caliendo, A. D'Amico, Hydrogen sensitivity of $Pd/SiO_2/Si$ structure: A correlation with the hydrogen-induced modifications on optical and transport properties of α-phase Pd films. *Sensors Actuators.* **16**, 43–54 (1989).
32. K. Von Rottkay, M. Rubin, P. A. Duine, Refractive index changes of Pd-coated magnesium lanthanide switchable mirrors upon hydrogen insertion. *J. Appl. Phys.* **85**, 408–413 (1999).
33. S. Wagner, T. Kramer, H. Uchida, P. Dobron, J. Cizek, A. Pundt, Mechanical stress and stress release channels in 10–350 nm palladium hydrogen thin films with different microstructures. *Acta Mater.* **114**, 116–125 (2016).
34. R. Delmelle, B. Amin-Ahmadi, M. Sinnaeve, H. Idrissi, T. Pardoen, D. Schryvers, J. Proost, Effect of structural defects on the hydriding kinetics of nanocrystalline Pd thin films. *Int. J. Hydrogen Energy* **40**, 7335–7347 (2015).
35. E. Lee, J. M. Lee, J. H. Koo, W. Lee, T. Lee, Hysteresis behavior of electrical resistance in Pd thin films during the process of absorption and desorption of hydrogen gas. *Int. J. Hydrogen Energy* **35**, 6984–6991 (2010).
36. T. A. Blank, L. P. Eksperiandova, K. N. Belikov, Recent trends of ceramic humidity sensors development: A review. *Sens. Actuators B Chem.* **228**, 416–442 (2016).
37. T. Satô, Y. Takeishi, H. Hara, Effects of crystallographic orientation on mobility, surface state density, and noise in *p*-type inversion layers on oxidized silicon surfaces. *Jpn. J. Appl. Phys.* **8**, 588 (1969).
38. Y. Sun, J. A. Rogers, Inorganic semiconductors for flexible electronics. *Adv. Mater.* **19**, 1897–1916 (2007).
39. S.-H. Hyon, W.-I. Cha, Y. Ikada, Preparation of transparent poly(vinyl alcohol) hydrogel. *Polym. Bull.* **22**, 119–122 (1989).
40. T. Das, X. Chen, H. Jang, I.-K. Oh, H. Kim, J.-H. Ahn, Highly flexible hybrid CMOS inverter based on Si nanomembrane and molybdenum disulfide. *Small* **12**, 5720–5727 (2016).

Acknowledgments: Part of the experimental work has been carried out in the Fudan Nanofabrication Laboratory. **Funding:** This work was supported by the National Natural Science Foundation of China (61975035, 51711540298, and 51925208), the Science and Technology Commission of Shanghai Municipality (17JC1401700), the National Key Technologies R&D Program of China (2015ZX02102-003), the Changjiang Young Scholars Program of China, and the Program of Shanghai Academic Research Leader (19XD1400600). T.L. acknowledges the support from the National Research Foundation of Korea (NRF) funded by the Ministry of Science and ICT (NRF-2017M3A7B4049466), the Yonsei-KIST Convergence Research Program and the Priority Research Centers Program through the NRF (NRF-2019R1A6A1A11055660). **Author contributions:** Y.M. designed this study. G.L., Z.M., and C.Y. fabricated and characterized the devices. G.L., J.X., and B.X. established the hydrogen testing system and measured the corresponding performance. G.L. and H.Z. established the moisture testing system and measured the corresponding performance. All authors discussed and analyzed the results. G.L., C.Y., and Y.M. wrote the paper. **Competing interests:** The authors declare that they have no competing interests. **Data and materials availability:** All data needed to evaluate the conclusions in the paper are present in the paper and/or the Supplementary Materials. Additional data related to this paper may be requested from the authors.

Submitted 27 September 2019
Accepted 12 February 2020
Published 1 May 2020
10.1126/sciadv.aaz6511

Citation: G. Li, Z. Ma, C. You, G. Huang, E. Song, R. Pan, H. Zhu, J. Xin, B. Xu, T. Lee, Z. An, Z. Di, Y. Mei, Silicon nanomembrane phototransistor flipped with multifunctional sensors toward smart digital dust. *Sci. Adv.* **6**, eaaz6511 (2020).

Science Advances

Silicon nanomembrane phototransistor flipped with multifunctional sensors toward smart digital dust

Gongjin Li, Zhe Ma, Chunyu You, Gaoshan Huang, Enming Song, Ruobing Pan, Hong Zhu, Jiaqi Xin, Borui Xu, Taeyoon Lee, Zhenghua An, Zengfeng Di and Yongfeng Mei

Sci Adv **6** (18), eaaz6511.
DOI: 10.1126/sciadv.aaz6511